Superconductor Science and Technology

PAPER • **OPEN ACCESS**

Magnetic granularity in pulsed laser deposited YBCO films on technical templates at 5 K

To cite this article: M Lao *et al* 2017 *Supercond. Sci. Technol.* **30** 104003

OPEN ACCESS
IOP Publishing
Superconductor Science and Technology
Supercond. Sci. Technol. **30** (2017) 104003 (8pp)
https://doi.org/10.1088/1361-6668/aa7f68

Magnetic granularity in pulsed laser deposited YBCO films on technical templates at 5 K

M Lao[1], J Hecher[1], P Pahlke[2], M Sieger[2], R Hühne[2] and M Eisterer[1]

[1] Atominstitut, TU Wien, Stadionallee 2, A-1020, Vienna, Austria
[2] Institute for Metallic Materials, IFW Dresden, Helmholtzstraße 20, D-01069, Dresden, Germany

E-mail: mlao@ati.ac.at

Received 28 April 2017, revised 10 July 2017
Accepted for publication 12 July 2017
Published 4 September 2017

Abstract

The manifestation of granularity in the superconducting properties of pulsed laser deposited YBCO films on commercially available metallic templates was investigated by scanning Hall probe microscopy at 5 K and was related to local orientation mapping of the YBCO layer. The YBCO films on stainless steel templates with a textured buffer layer of yttrium stabilized ZrO_2 grown by alternating beam assisted deposition have a mean grain size of less than 1 μm with a sharp texture. This results in a homogeneous trapped field profile and spatial distribution of the current density. On the other hand, YBCO films on biaxially textured NiW substrates show magnetic granularity that persists down to a temperature of 5 K and up to an applied magnetic field of 4 T. The origin of the granular field profile is directly correlated to the microstructural properties of the YBCO layer adopted from the granular NiW substrate which leads to a spatially inhomogeneous current density. Grain-to-grain in-plane tilts lead to grain boundaries that obstruct the current while out-of-plane tilts mainly affect the grain properties, resulting in areas with low J_c. Hence, not all grain boundaries cause detrimental effects on J_c since the orientation of individual NiW grains also contributes to observed inhomogeneity and granularity.

Keywords: coated conductors, critical current density, SHPM, trapped field, granularity, YBCO

(Some figures may appear in colour only in the online journal)

1. Introduction

The growing demand to generate large magnetic fields with $(RE)Ba_2Cu_3O_{7-\delta}$ (RE = rare earth element, REBCO) compounds calls for the optimization of their current carrying capacity especially at low temperatures. REBCO materials are grown on metal-based templates with well-aligned grains which are known as coated conductors (CCs), where large self-field critical current densities, $J_c > 1$ MA cm^{-2} at 77 K have been achieved. Two main routes for CC production have been established: (i) the use of rolling assisted biaxially textured substrates (RABiTS) of Ni-based alloys [1, 2] and (ii) growth of textured buffer layers either by ion/alternating beam assisted deposition (IBAD/ABAD) on Hastelloy or stainless steel (SS) substrates [3, 4] or by inclined substrate deposition on Hastelloy tape [5]. These methods induce a preferential growth direction of the grains and inhibit the formation of high-angle grain boundaries that drastically reduce the global J_c. At present, CCs have grain boundary (GB) misorientation angle, θ_{GB}, below 10°, which are referred to as low angle grain boundaries (LAGB) [6]. Additional nano-engineering of the vortex pinning landscape can enhance J_c and reduce its anisotropy in magnetic fields. However, the performance of pinning centers and the suppression of the global J_c by GBs especially at temperatures below 77 K are still one of the open issues in the development of CCs.

The critical current density is known to decrease exponentially with increasing θ_{GB}. Transport J_c studies conducted by D

Verelbeyi *et al* on isolated GBs on IBAD and RABiTS tapes show that the exponential decrease starts at a critical angle, θ_c, of about 4° [7]. Magneto-optical (MO) studies done by Feldmann *et al* complemented by local misorientation mapping of NiW substrates, have shown that flux penetration starts at the edges of the sample and propagates along weak-linked regions [8, 9]. The flux penetrated areas in the MO-images correspond directly to grain-to-grain interfaces with $\theta_{GB} \geqslant 4°$—a value consistent to the θ_c found in transport measurements. The dependence of the global J_c on the applied magnetic field for isolated GB samples with low misorientation angles was found to approach the single grain J_c dependence upon increasing the applied field. This implies that the effect of the GBs on the global J_c becomes negligible at larger fields [7] and the intragrain J_c has the dominant limiting effect. One can then focus on optimizing the pinning landscape and neglect the effects of LAGBs at high fields which has been done extensively especially at 77 K. However, as the temperature is decreased, the magnetic field range in which LAGBs start to limit J_c and the definite transition between the GB-limited J_c and grain-dominated J_c becomes ambiguous.

In this paper we present the significance of granularity and local texture on the critical current density at low temperatures of pulsed laser deposited YBCO on two types of technical substrates. Pulsed laser deposition (PLD) is known to be a reliable deposition route where YBCO films with large critical current densities have been achieved. The grain boundaries are planar and it enables similar growth conditions of YBCO on the two types of metallic templates. To study the effects of granularity, we use scanning Hall probe microscopy (SHPM) to image magnetic field profiles above superconducting tapes. It was proven to be a superior method to investigate the behavior of both intra- and intergranular J_c such as in polycrystalline samples of iron-based superconductors [10]. The SHPM used in this study enables in-field measurements up to 5 T. Information on grain misorientations and GB angles was provided by electron backscatter diffraction (EBSD) maps of the YBCO layer. The combination of both methods enables the study of the effects of granularity on J_c.

2. Experimental details

The YBCO layer was grown via PLD using a KrF excimer laser (COHERENT LPXpro 305, $\lambda = 248$ nm) with an energy density of 1.6 J cm^{-2} at the target surface. Two types of technical templates were used. The first is based on a RABiTS Ni-5 at%W (NiW) buffered with chemically deposited $La_2Zr_2O_7$ (LZO) and CeO_2 layers. The second consists of a SS substrate with yttrium stabilized ZrO_2 (YSZ) grown by ABAD and PLD-CeO_2 as buffer layers. The thickness of the YBCO layer in both types of samples is about 1.5 μm and they will be referred to as YBCO-NiW and YBCO-SS for the films on NiW and SS substrates, respectively. Small circular spots were patterned by wet chemical etching to facilitate a local analysis of the superconducting layer and better comparability between the field profiles, EBSD maps and electron microscopy images. The etched spots have a diameter of about 450 μm. To compare with the CCs, PLD-YBCO films were also grown on bicrystal $SrTiO_3$ with [001]-tilt and misorientation angles of 4° and 12°.

The magnetic field profiles were measured using a scanning Hall probe microscope equipped with a high-resolution Hall effect sensor. The Hall probe was mounted on a cantilever made of a carbon sheet. The distance control between the sample and the Hall sensor was tracked from a change in the voltage of a Wheatstone bridge assembly that includes two strain gauges attached to the cantilever. The scanning position was adjusted by three piezo-positioners for the x, y and z-directions. The whole sample-holder was installed in a helium gas flow cryostat equipped with an 8 T superconducting magnet. The temperature in the sample space can be stabilized between 3 and 300 K. The magnetic field was applied perpendicular to the sample surface for all measurements. All SHPM data were obtained after zero-field cooling. The remanent field profiles were measured after applying magnetic fields $\geqslant 2H^*$, where H^* is the sample's full penetration field and is typically in the range of 0.5–2 T at 5 K. Magnetic relaxation in the remanent state was minimized by reducing the temperature by 1 K after magnetization (undercooling). The minimum spatial resolution was about 2 μm with a similar distance, d, of the Hall probe to the sample surface.

An algorithm for the inversion of the Biot–Savart law was utilized to calculate the spatial distribution of J_c from the measured $B_z(x, y)$ [11]. Due to the thin-film geometry of the sample, the current flow is assumed to be planar and z-independent.

The grain orientation and GB angles were investigated by EBSD measurements using a GEMINI LEO 1530 SEM with a Nordlys EBSD detector. The details of the acquisition procedure and post-processing of EBSD patterns are described elsewhere [12]. Scanning electron microscopy (SEM) images were acquired using a JEOL JSM-6510 at an acceleration voltage of 20 kV.

3. Results

The EBSD images of the YBCO layer of the YBCO-NiW and YBCO-SS samples are presented in figures 1(a) and (b). The granular morphology of the NiW template is transferred to the PLD-grown YBCO layer and grain sizes of 20–50 μm are clearly seen (figure 1(a)). In YBCO-NiW, θ_{GB} ranges from 1.5°–10°. Within a NiW grain, the YBCO layer has a subgrain structure made up of much smaller grains wherein the misorientations are below 3°. On the other hand, the blue lines in the EBSD map of YBCO-SS (figure 1(b)) depict small grains with sizes below 1 μm and θ_{GB} less than 3°. On a length scale of a few micrometers, the subgrain structure in YBCO-NiW and YBCO-SS appear similar and both are also porous. The misorientation with respect to the ideal cube texture is visualized by the gradient from white to black. The texture is more homogeneous in YBCO-SS and it varies for each grain in YBCO-NiW. The imperfect texture of YBCO-NiW arises from the misorientation of the underlying NiW grains. As a result of the PLD growth, the YBCO layer is also slightly

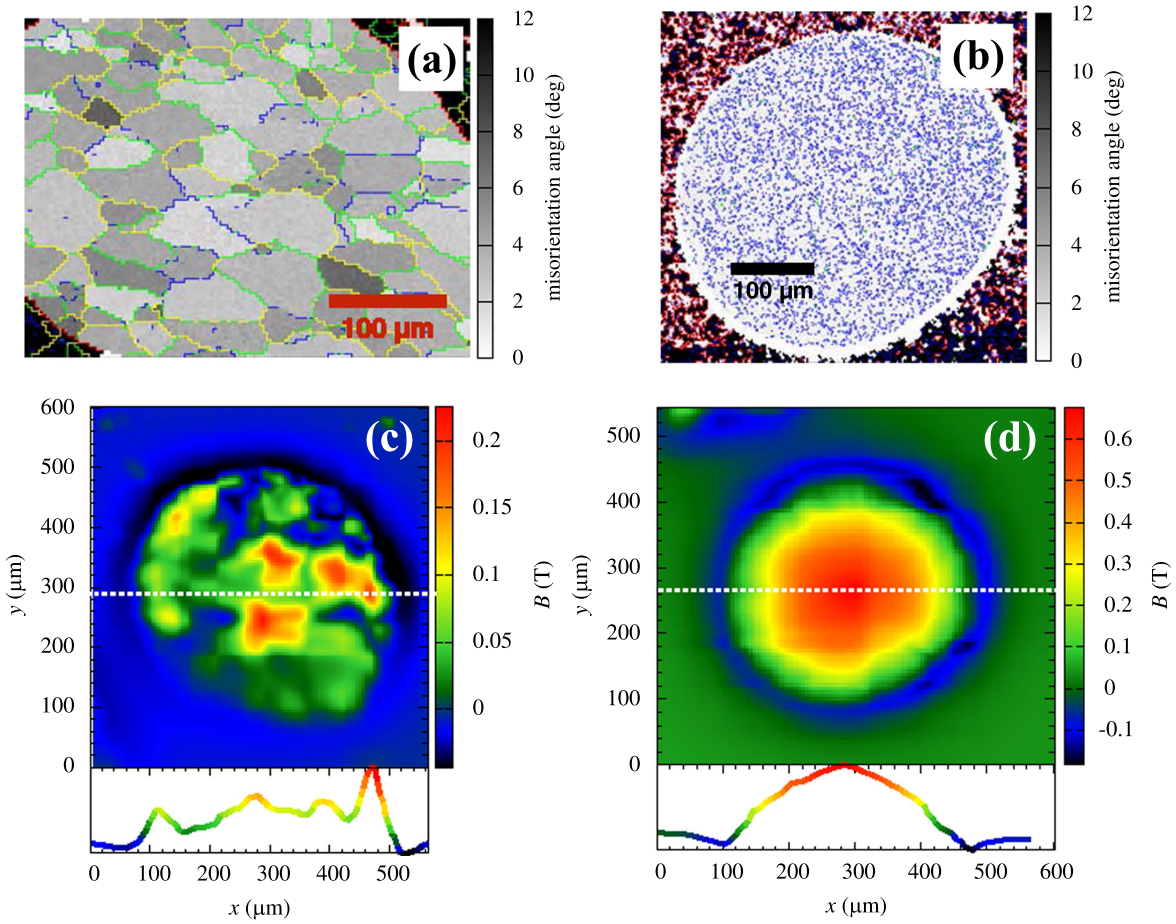

Figure 1. EBSD images of (a) YBCO-NiW and (b) YBCO-SS. The colored lines denote θ_{GB} with the following definitions: blue → $\theta_{GB} = 1.5°$–$3°$, green → $\theta_{GB} = 3°$–$6°$, yellow → $\theta_{GB} = 6°$–$12°$ and red → $\theta_{GB} > 12°$. The color gradient from white to black indicates the average misorientation from the ideal cube texture. Remanent field profile of (c) YBCO-NiW and (d) YBCO-SS at 5 K. The Hall probe-sample distance was approximately 4 μm and the scanning step width was 5 and 4 μm in the x and y-directions, respectively. The white dashed lines indicate positions of the line scans below each map.

misoriented. The porosity of the YBCO layer also varies from grain to grain of the NiW substrate as a consequence of the individual facetation of each NiW grain, which is similar to findings in YBCO films on vicinal $SrTiO_3$ substrate [13, 14]. It was observed in SEM images of the bare NiW template that some grain boundaries of NiW form trenches. These lead to the formation of step-like structures in the GBs of the YBCO layer. Thus, some GBs appear smooth while others are grooved. A thorough discussion about the microstructure of the YBCO layer in relation to the underlying templates can be found in [12].

Figures 1(c) and (d) shows the remanent field profiles of the same area as the EBSD images. The differences in the granular characteristics of the two samples are manifested in the field maps. In YBCO-NiW (figure 1(c)), magnetic grains are formed with widths of up to ≈120 μm and they correspond to a cluster of strongly connected YBCO grains. The strength of the signal of each magnetic grain varies and some parts outside the large clusters penetrate a very small to almost zero field. It is desirable to correlate the microstructure of each YBCO grain to the variation in the local magnetic signal and the formation of magnetic grains. This will be discussed later.

The trapped field in YBCO-SS has a more uniform shape (figure 1(d)) depicting a homogeneous current. It is possible that the granularity is not resolved by the Hall mapping since the spatial resolution of the measurement is larger than the YBCO grain size. Nevertheless, the shape of the profile is evidently more homogenous than the one above the YBCO-NiW. The peak of the trapped field is 0.67 T in YBCO-SS, which is more than three times the local maximum field above YBCO-NiW (0.2 T).

In-field line scans of the field profile above YBCO-NiW and YBCO-SS at $T = 5$ K are shown in figures 2 and 3. The granularity in the profile of YBCO-NiW (figure 2) persists up to 4 T implying the significance of granularity at this temperature and up to this applied field. The field profile does not converge to a global profile that would depict a suppression of granularity at higher fields. Only a decrease in the peak of each magnetic grain is observed above 0.5 T, which corresponds to the expected decrease of J_c with field. However, an interesting behavior is observed between the profiles of the remanent state and at 0.2 T. The peaks do not follow a monotonic decrease which was observed in all samples where granularity is pronounced. Such a behavior seems to be consistent to the well-known field dependence of transport

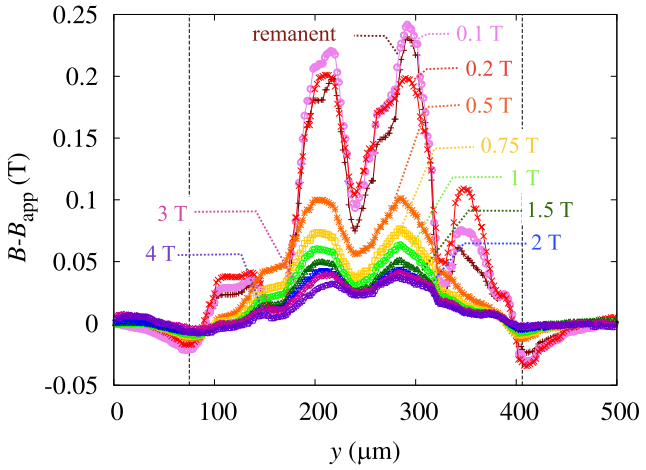

Figure 2. Line scans of the field profile above YBCO-NiW at $T = 5$ K and different applied magnetic fields. The data were taken in decreasing field after ramping the magnetic field to 5 T. The step width and distance of the Hall probe to the sample surface were about 2 μm. The vertical dashed lines indicate the edges of the sample. The applied field is subtracted from the data.

current across bicrystal YBCO films with low θ_{GB}. As reported in previous studies [7, 15], grain boundaries typically have a smaller J_c compared with the intragrain J_c at low fields. The intergrain J_c converges with the grain-like behavior at higher fields. Therefore, the observed changes of the shape of the field profile from zero to 0.2 T may reflect transition from GB-limited J_c to grain-limited behavior as more GBs become transparent to the current (i.e. less GBs suppress the currents locally).

The line scan across the center of the circular spot of YBCO-SS has an asymmetric shape and a dent (denoted by the black arrows in figure 3(a)) which are visible at all applied fields. The imperfections signify local inhomogeneities such as microcracks, nonstoichiometry and precipitates. The overall decrease of B_{peak} is consistent with the expected decrease of J_c with increasing H_{app}. When all the experimental data are normalized as shown in figure 3(b), the broadening of the peak observed at the remanent state and 0.2 T disappears and the shape of the field profiles approaches the calculated curve for a constant J_c (dashed blue curve) as the field increases. The broadening of the peak at lower fields is a manifestation of the field dependence of J_c, which becomes weaker at higher fields. Additional differences of the experimental data to the constant J_c curve include the local suppression around the defect (indicated by the red arrow) and the deviation from the sharp maximum at the center which is probably an effect of nonlinear flux diffusion and reflects the gradient of the electric field, E, towards the center of the sample [16].

4. Discussion

Figure 4 shows the spatial distribution of the critical current density of YBCO-SS evaluated from its field map at 5 K. The average self-field J_c based on the current map is about 30 MA cm^{-2} which is consistent with the J_c of a similarly prepared sample measured by magnetometry. The superimposed vector field on the J_c-map corresponds to the direction of the current and it depicts a uniform circular flow. The monotonic decrease of J_c from the edges towards the center of the sample (red curve in the right panel of figure 4) again illustrates the influence of the local dependence of J_c on B deduced from the field profile in the previous section. This behavior becomes weaker at 1 T (black dotted–dashed curve). The minimum at the center is due to an almost zero E as the area enclosed by the circulating current becomes infinitesimally small.

The spatial distribution of J_c in YBCO-NiW is shown in figure 5(a). Unlike in YBCO-SS, $J_c(x, y)$ is inhomogeneous as an obvious consequence of its granular field profile. All GBs are visualized and each line color indicates a specific range of θ_{GB} determined via EBSD. The solid and dashed lines represent smooth and grooved GBs resolved by SEM. The black arrows depict the current vector field. Areas with locally degraded J_c are found to correlate with the appearance of the YBCO layer in the SEM images. The grooved GBs, which also lead to the formation of precipitates, cause a local degradation in J_c as shown for example by the two boxed areas numbered 1 and 2 in figure 5(b) and their corresponding SEM images in figures 5(c) and (d). A segregation of precipitates that appear white is found around the GB in figure 5(c). This corresponds to the local degradation of J_c in the area denoted by #1 in figure 5(b). On the other hand, the boundary indicated in area #2 has a pronounced grooving (figure 5(d)) and evidently blocks the currents. In addition, some grains that are more porous, which is attributed to the faceted surface of the NiW substrate, have lower J_c as illustrated by box #3 in figure 5(b) and the backscatter electron image in figure 5(e).

The simultaneous analysis of current maps and local orientation mapping shows that not all GBs suppress the current flow, even those with $\theta_{GB} > 6°$ shown in figure 5(b). If a GB blocks the current, it is expected that the currents flow in opposite directions at both sides of the boundary such as in YBCO films grown on bicrystal substrate with in-plane misorientation (figure 6). Similar results were obtained for 4° and 12°-misoriented boundaries. However this is evidently not the case for most GBs in YBCO-NiW even those with large misorientation. The current seem to pass them in most of the cases except for a few instances such as the 9°—GB indicated by the red arrow in figure 5(b).

To gain further insight on the significance of the GBs on the inhomogeneity of J_c, the types of GB tilt are considered. The kind of misorientation can be determined by considering a cut from the EBSD map separating the angular deviations from the [001], [010] and [100] YBCO axes with respect to the rolling, transverse and normal directions of the tape, respectively (see figure 7(a)). Similar to the findings of P Pahlke *et al* [12] on a CC with a Ni-9at%W substrate, figure 7(b) shows that in YBCO-NiW not all axes are always correlated suggesting the absence of a preferred axis of rotation. If two axes are correlated, the axis of rotation is about the third uncorrelated axis. Therefore, the type of GB can be identified either as [100]-twist,

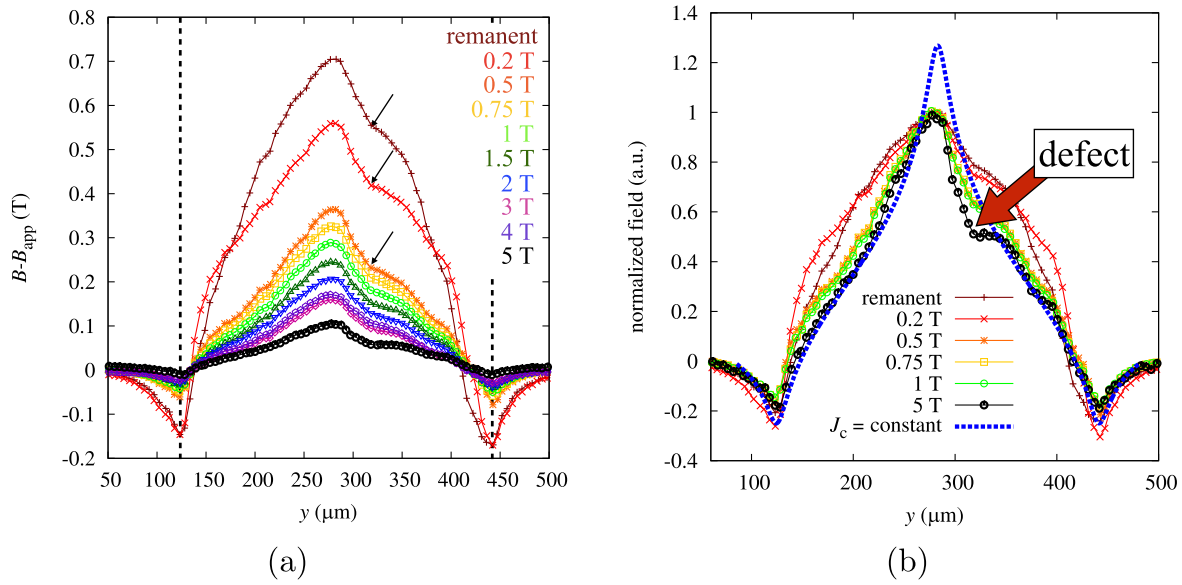

Figure 3. Field profiles above YBCO-SS at $T = 4$ K and different applied magnetic fields. The data were taken in decreasing field. The step width and distance of the Hall probe to the sample surface were about 2 μm. The vertical dashed lines indicate the edges of the sample. (b) Normalized $B(y)$ to show how the shape of the field profile evolves with field. The blue dashed curve corresponds to the theoretical field profile assuming a constant J_c. It is fitted to the data at $\mu_0 H_{app} = 5$ T. The applied field is subtracted from the data.

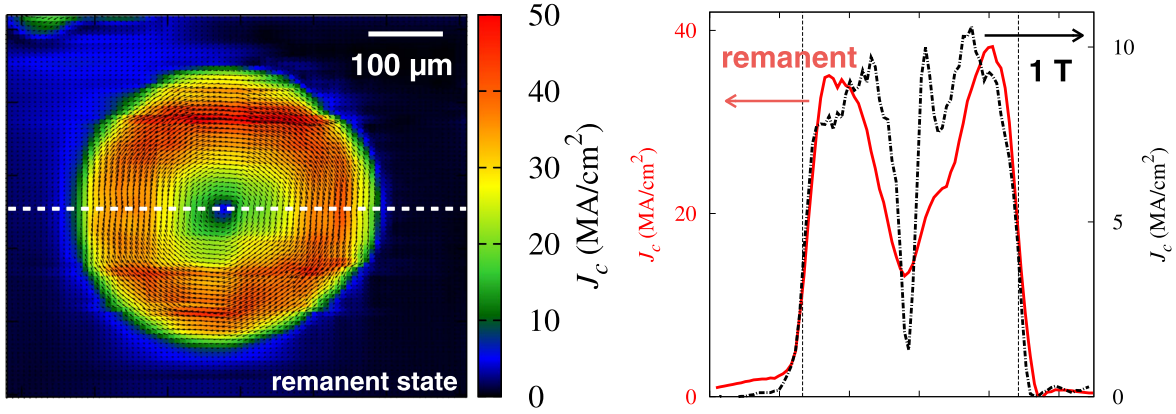

Figure 4. Critical current density map (left) evaluated from the field profile of YBCO-SS. A vector field that indicates the current flow is superimposed to the current maps. The white dashed horizontal line depicts the position of the cut in the right panel comparing the J_c-profile at the remanent state and in an applied field of 1 T.

[001]-tilt or [010]-tilt type. This is further illustrated by the diagram in figure 7(c). Held *et al* have conducted a comprehensive study on the transport current across these types of GBs and they found that the [001]-tilt type has the most detrimental effect on J_c [17].

Figure 8 shows cuts of the remanent field, J_c and EBSD maps taken from two parts of the sample. Important points are revealed regarding the role of GBs and local misorientation. In figure 8(a), the magnetic clusters I and II are indicated. In cluster II, the gray shaded region corresponds to a low J_c area and EBSD reveals that this region consists of small grains having [001]-tilt type boundaries. In addition, the grains' misorientation angle are relatively large including a $9° - \theta_{GB}$. Hence, J_y is almost zero. The grains also have an out-of-plane tilt of about 5° which also causes an overall degradation of J_c in the x-direction. Grain boundaries A and B which are both of [001]-tilt type are indicated having zero J_y. On the other hand, the GBs within cluster I (shaded with pink) have an overall [010]-tilt and a reduction on J_y is observed due to the out-of-plane tilt, but they do not show current blockage. Furthermore, the gray shaded region in figure 8(b) is another cluster enclosing [100]-twist type boundaries. The zero J_c denoted by the blue arrow corresponds to the center of the circulating current, but the overall reduction of current between the dashed vertical lines is likely caused by the large out-of-plane tilt of about 6°. The GBs marked C and D were selected since both are greater than 6°. Both of these boundaries are [100]-twist type with C having a small in-plane tilt. There is again no indication of current obstruction for this type of boundary.

Evaluating the spatial distribution of J_c from the field map is a two-dimensional problem making such an analysis of the line scans tricky in some cases. However, important points are still revealed which includes the overall degradation of local J_c

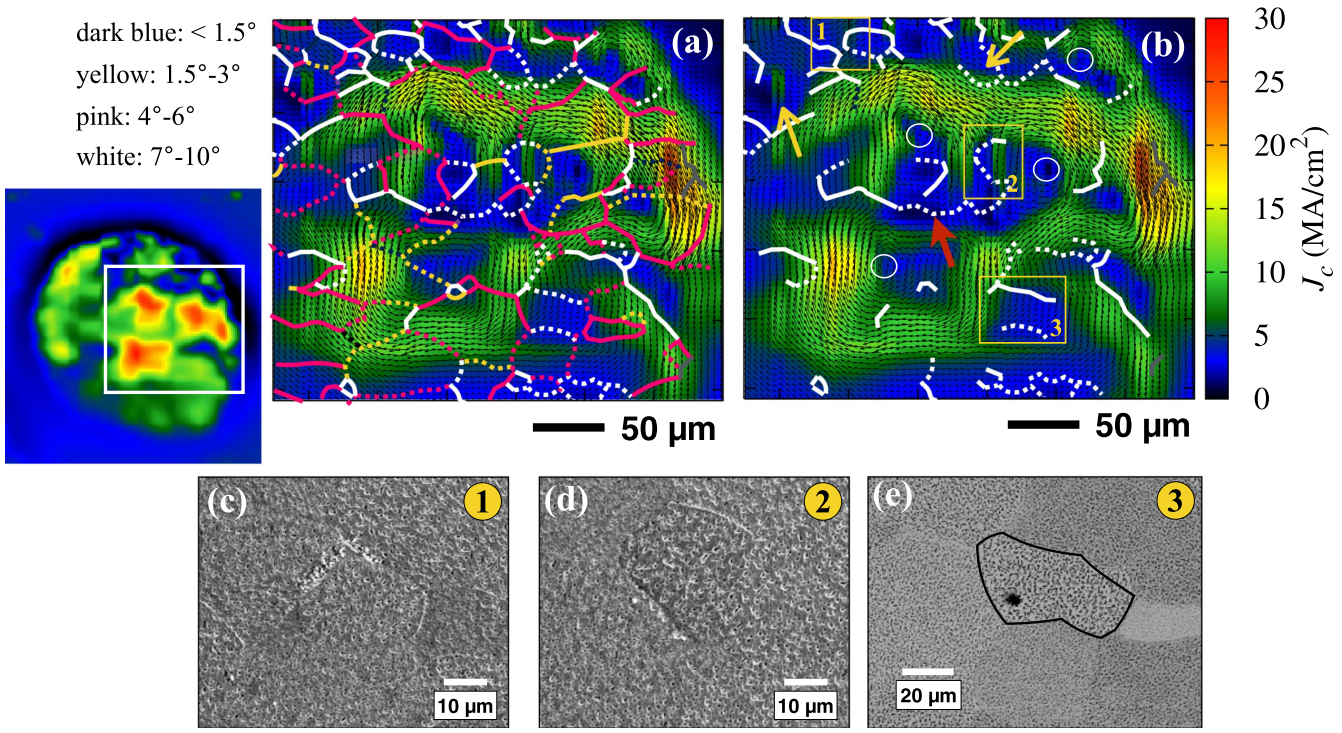

Figure 5. Critical current density map of YBCO-NiW superimposed with (a) all GBs and (b) only GBs with $\theta_{GB} > 6°$. The solid and dashed GB line correspond to the smooth and grooved GBs, respectively. The inset on the left is the remanent field map where the area enclosed by the box corresponds to the area of the J_c maps. The encircled areas in (b) denote a corresponding local maximum in the $B(x, y)$ while the red arrow indicates grooved GB with $\theta_{GB} = 9°$. (c), (d) SEM images and (e) backscatter electron image corresponding to the boxed areas in (b). The black border is drawn to emphasize the grain.

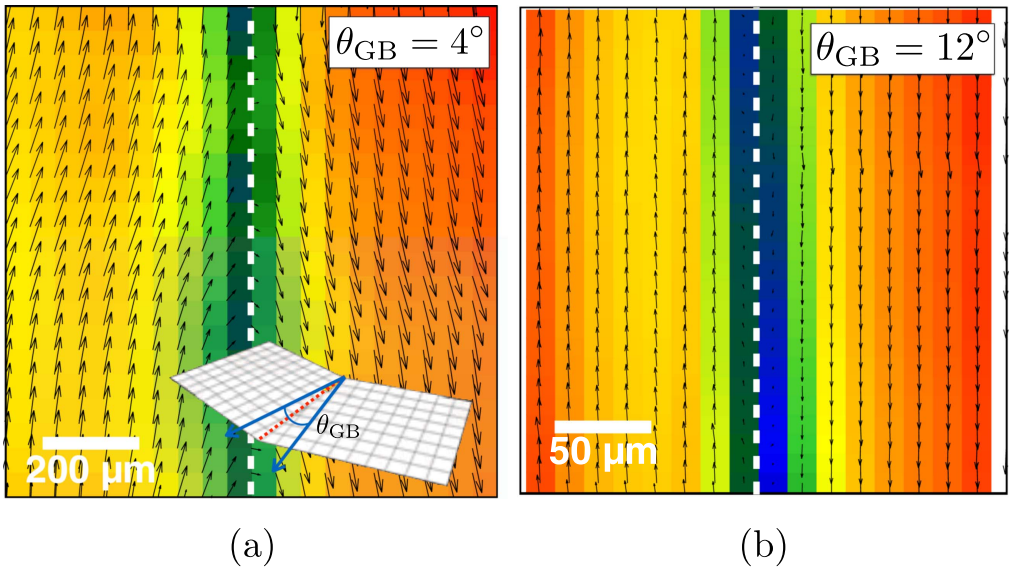

Figure 6. Current density map of YBCO films on bicrystal substrate with misorientation angle of (a) 4° and (b) 12°. The inset in (a) shows a schematic of the boundary with in-plane tilt.

associated to the local out-of-plane tilts of the YBCO axes. Some GBs, even with higher misorientation angle, do not block and degrade the current, depending on the GB type. This difference in the capability of transporting currents between different GB types may also provide additional insight in the critical current variation in GBs with high misorientation angle —the so-called Josephson junctions [18].

5. Conclusions

The influence of the template architecture on the microstructure and superconducting properties of PLD-grown YBCO films was investigated. Two commercial templates were used for this purpose: a RABiTS Ni-5 at%W and a SS tape with an ABAD-textured YSZ buffer layer. The YBCO

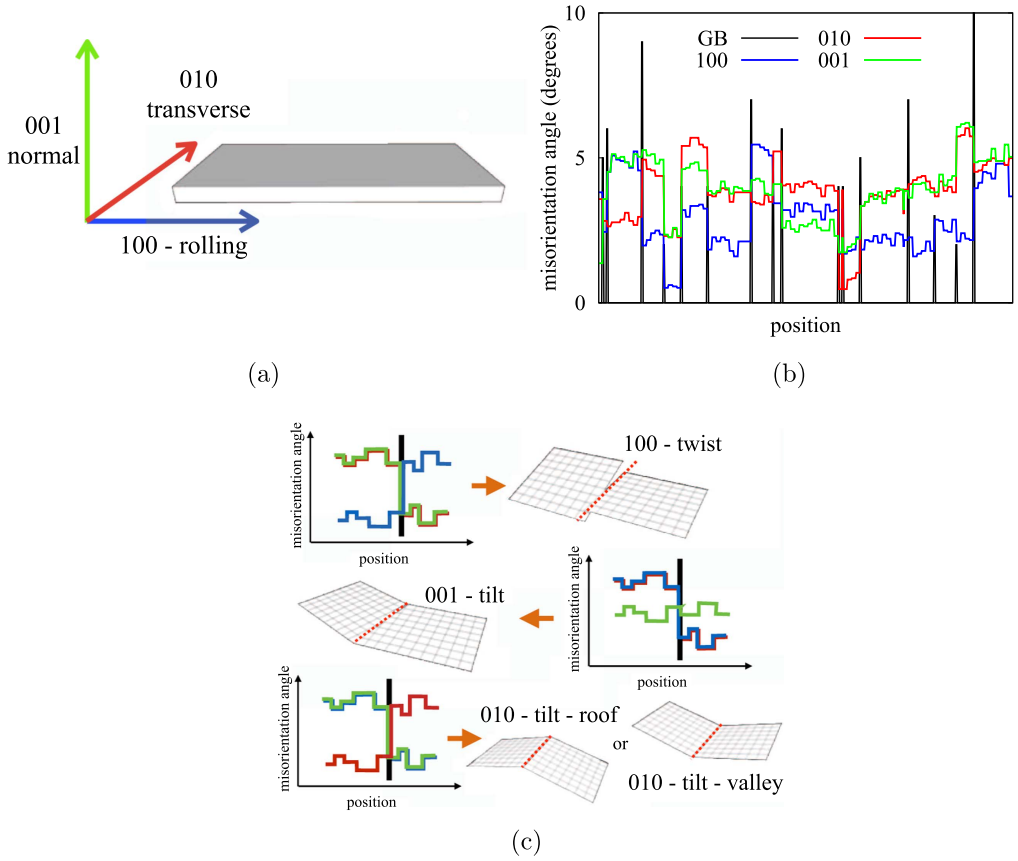

Figure 7. (a) Definition of the main directions of the tape. (b) EBSD line scan of YBCO-NiW. (c) Illustrations of the [100]-twist, [001]-tilt and [010]-tilt types deduced from the EBSD line scans.

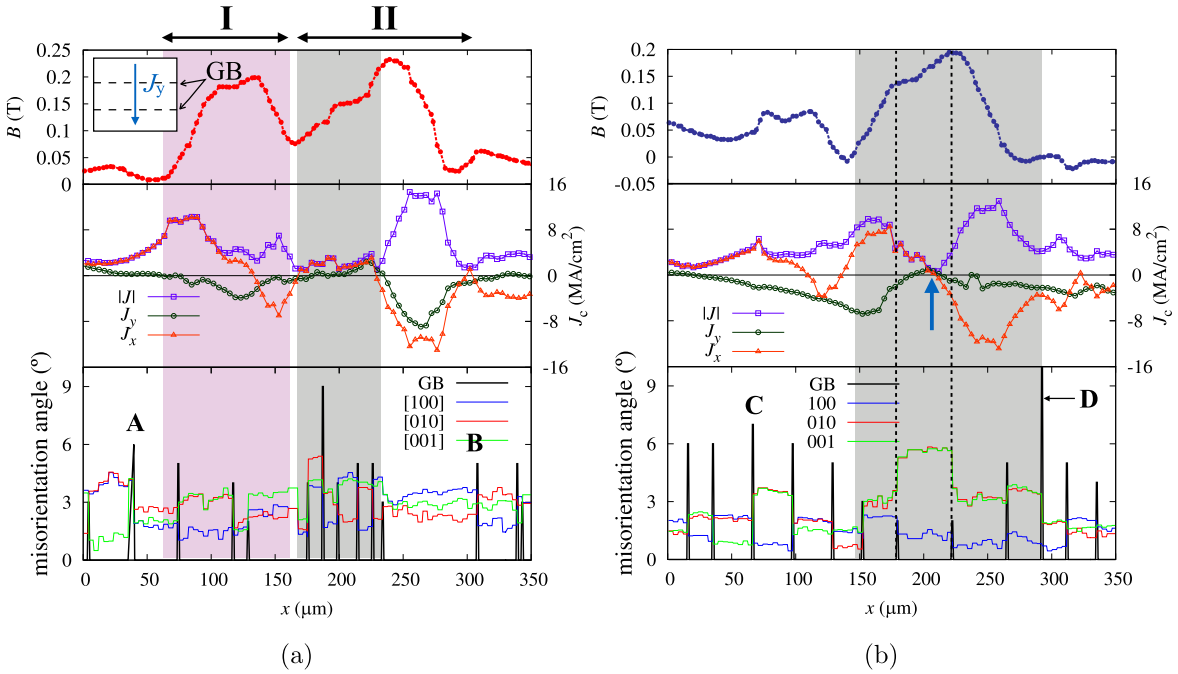

Figure 8. Cuts of the remanent field (top), J_c (middle) and EBSD (bottom) maps of YBCO-NiW. The two data sets refer to positions (a) $x = 300$ μm and (b) $x = 400$ μm in figure 1(c). The inset in the upper panel of (a) illustrates that J_y refers to the component of the current that crosses the GBs plotted as black solid lines in the EBSD line scans.

film on the ABAD-textured template has grain sizes of less than 1 μm and the in-plane misorientations are below 3°. As a result, a homogenous field profile was resolved using SHPM at 5 K. On the other hand, a significant magnetic granularity was revealed in the tape with NiW substrate. The granularity was found to persist up to 4 T. The texture and microstructural features of the YBCO layer leading to the observed inhomogeneity in both the field profile and corresponding current density maps were identified. It was found that spatial inhomogeneities in the YBCO layer such as local porosity, grooving along the boundaries and segregation of the secondary phases cause the local degradation of J_c. In-plane misorientation leads to [001]-tilt type grain boundaries which obstruct the current flow, while out-of-plane tilt directly affects the grain properties and cause lower J_c areas. Not all grain boundaries, even those with misorientations between 6° and 10°, inhibit the current flow since the type of GB tilt ([001]-tilt) must be taken into consideration. These results entail that it is important to minimize local variation of the cube texture and granularity in the metallic template, as in the case of RABiTS, since these properties potentially cause degradation in the current conducting properties. From this point of view, an overall improvement in the template is beneficial for CCs both in RABiTS and ABAD-buffered templates.

Acknowledgments

The authors would like to thank A Usoskin (Bruker HTS GmbH) for the provision of ABAD-YSZ buffered stainless steel templates and M Falter (Deutsche Nanoschicht GmbH) for the buffered NiW tape. The authors acknowledge the TU Wien university library for financial support through its open access funding program. This work was supported by EUROTAPES which has received funding from European Union Seventh Framework Programme [FP7/2007-2013] under grant agreement no. NMP-LA-2012-280432.

References

[1] Goyal A, Paranthaman M P and Schoop U 2004 *MRS Bull.* **29** 552
[2] Gaitzsch U, Hänisch J, Hühne R, Rodig C, Freudenberger J, Holzapfel B and Schultz L 2013 *Supercond. Sci. Technol.* **26** 085024
[3] Usoskin A, Kirchhoff L, Knoke J, Prause B, Rutt A, Selskij V and Farrell D E 2007 *IEEE Trans. Appl. Supercond.* **17** 3235–8
[4] Yu L S, Harper J M E, Cuomo J J and Smith D A 1985 *Appl. Phys. Lett.* **47** 932
[5] Dürrschnabel M, Aabdin Z, Bauer M, Semerad R, Prusseit W and Eibl O 2012 *Supercond. Sci. Technol.* **25** 105007
[6] Durrell J H and Rutter N A 2009 *Supercond. Sci. Technol.* **22** 013001
[7] Verebelyi D T *et al* 2000 *Appl. Phys. Lett.* **76** 1755–7
[8] Feldmann D M *et al* 2000 *Appl. Phys. Lett.* **77** 2906–8
[9] Feldmann D M *et al* 2001 *IEEE Trans. Appl. Supercond.* **11** 3772–5
[10] Hecher J, Baumgartner T, Weiss J D, Tarantini C, Yamamoto A, Jiang J, Hellstrom E E, Larbalestier D C and Eisterer M 2016 *Supercond. Sci. Technol.* **29** 025004
[11] Hengstberger F, Eisterer M, Zehetmayer M and Weber H W 2009 *Supercond. Sci. Technol.* **22** 025011
[12] Pahlke P, Sieger M, Chekhonin P, Skrotzki W, Hänisch J, Usoskin A, Strömer J, Schultz L and Hühne R 2016 *IEEE Trans. Appl. Supercond.* **26** 7201505
[13] Emergo R L S, Wu J Z, Aytug T and Christen D K 2004 *Appl. Phys. Lett.* **85** 618
[14] Sieger M *et al* 2017 *IEEE Trans. Appl. Supercond.* **27** 7500504
[15] Heinig N F, Redwing R D, Nordman J E and Larbalestier D C 1999 *Phys. Rev.* B **60** 1409
[16] Lao M, Hecher J, Sieger M, Pahlke P, Bauer M, Hühne R and Eisterer M 2017 *Supercond. Sci. Technol.* **30** 024004
[17] Held R, Mannhart J C W S, Allard L E, More K L and Goyal A 2009 *Phys. Rev.* B **79** 014515
[18] Tafuri F, Kirtley J R, Lombardi F, Medaglia P G, Orgiani P and Balestrino G 2004 *Low Temp. Phys.* **30** 591